Steady flow around an inclined torus at low Reynolds numbers: Lift and drag coefficients

Yu Peng[1], Ruixin Lu[1], Wei He[1,2], Larry K.B. Li[2]

Abstract

The steady flow around an inclined torus has received little attention, despite being relevant to many engineering and biological situations, such as the sedimentation of fluidized particles and the motion of natural micro-swimmers. In this study, we perform three-dimensional direct numerical simulations of the flow around an inclined torus over a range of aspect ratios ($2 \leqslant Æ \leqslant 3$), inclination angles ($0 \leqslant \theta \leqslant 90°$) and Reynolds numbers ($10 \leqslant Re \leqslant 50$), with a focus on the steady flow regime preceding the onset of vortex shedding.

For a fixed Re, we find that as the torus inclines from a flow-normal orientation ($\theta = 0°$) to a flow-parallel orientation ($\theta = 90°$), the drag coefficient (C_D) decreases monotonically, while the lift coefficient (C_L) first increases from zero, reaches a maximum at $40° \leqslant \theta \leqslant 50°$ and then returns to zero owing to top-down symmetry at full inclination. The decrease in C_D with θ is caused by a decrease in the pressure drag, with almost no change in the viscous drag. The variation in C_L with θ is caused by the pressure lift dominating the viscous lift. With increasing Re, the overall trends in C_D and C_L remain qualitatively unchanged but their quantitative values decrease. Compared with the effects of θ and Re, those of $Æ$ are relatively weak for the specific flow conditions examined here. We conclude by performing a nonlinear regression analysis to generate curve fits for C_D and C_L in terms of $Æ$, θ and Re.

Keywords: Wakes, bluff-body flows, torus, recirculation zone, direct numerical simulations

1. Introduction

The flow around three-dimensional (3D) bluff bodies has been the subject of decades of analytical, numerical and experimental research [1]. However, these flows continue to attract attention owing to their significance in a wide range of established and emerging fields, such as the sedimentation of fluidized particles and fibers [2] and the active control of flow instabilities [3]. Two of the most widely studied wake flows are those from a circular cylinder [4] and from a sphere [5]. However, the flow around a torus, which is the geometrical intermediate between a cylinder and a sphere, has been less well studied, despite being

[1]Department of Mechanics and Aerospace Engineering, Southern University of Science and Technology, Shenzhen, China

[2]Department of Mechanical and Aerospace Engineering, The Hong Kong University of Science and Technology, Clear Water Bay, Hong Kong

prevalent in many engineering and biological situations, such as the flow around helical heat exchangers [6] and the motion of natural micro-swimmers such as helical flagella [7].

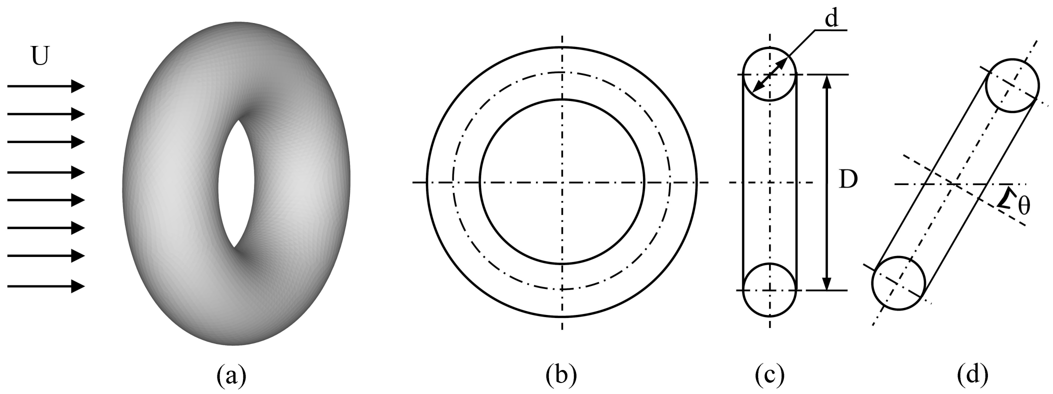

Fig. 1: Schematic of a torus in a uniform free-stream: (a) 3D view, (b) front view, (c) side view at zero inclination, and (d) side view at an inclination angle of θ.

Figure 1 shows the geometry of a typical torus. Its aspect ratio is defined as $A\!\!R \equiv D/d$, where d is the cross-sectional diameter of the torus and D is its centerline diameter. The torus becomes a sphere as $A\!\!R \to 0$ but becomes a circular cylinder as $A\!\!R \to \infty$ [8]. Therefore, by studying the flow around a torus at intermediate aspect ratios, one can gain insight into the connection between sphere wakes ($A\!\!R = 0$) and cylinder wakes ($A\!\!R = \infty$). In such bluff-body wakes, it is well known that a series of bifurcations occurs as the Reynolds number (Re) increases, taking the flow from a steady creeping state at $Re \sim 1$ [9] to an unsteady 3D state at a higher Re whose exact critical value depends on the subtle details of the bluff-body geometry [10, 11]. In the rest of this introduction, we will review the key features of these classical wakes at different Reynolds numbers, before presenting our case for the need to study torus wakes further, particularly when the Reynolds number is low and when the torus is inclined relative to the oncoming free-stream, as illustrated in Fig. 1(d).

1.1. Flow around a sphere ($A\!\!R = 0$)

For the flow around a sphere, the creeping solution at $Re \sim 1$ can be found through the analytical method of Stokes [12, 13] or Oseen [14, 15]. As Re increases from ~ 1, the flow remains steady but develops an axisymmetric recirculation zone when Re reaches ≈ 20–24, as shown in the experiments of Taneda [9] and Wu & Faeth [16]. Numerical simulations by Fornberg [17] have shown that the length of the recirculation zone increases with $\log(Re)$ until a symmetry-breaking bifurcation occurs at $Re \approx 210$. The onset of that bifurcation is consistent with the stability analysis of Natarajan & Acrivos [18] and the numerical simulations of Johnson & Patel [10] and Tomboulides & Orszag [11], which showed that the flow at $210 < Re < 270$ is still steady but no longer axisymmetric. At $Re = 277.5$, stability analyses predict another bifurcation, but this time to an unsteady limit cycle [18]. This has been confirmed by numerical simulations showing the onset of unsteady flow at $Re > 280$, with periodic vortex shedding occurring above $Re \approx 300$ [10, 11].

In addition to the wake structure and its dynamics, the drag coefficient and its variation with Re are also important considerations, e.g. in the analysis of sedimentation and microbiological flows [19]. Several experimental and numerical studies have been conducted to determine the drag coefficient of a sphere at different Reynolds numbers [5, 20]. The main findings are that the drag coefficient (i) decreases as Re increases from ~ 1 to around 350 because of a transition from viscous-dominated flow to pressure-dominated flow, but that it (ii) remains relatively constant at higher Re until the onset of boundary-layer transition at $Re \sim \mathcal{O}(10^5)$ [10, 11]. A comprehensive list of the empirical and semi-empirical correlations that have been proposed for the drag coefficient of a sphere can be found in Ref. [5].

1.2. Flow around a cylinder ($\mathcal{AR} = \infty$)

For the flow around a circular cylinder, Underwood [21] has shown that the critical Reynolds number at which a steady recirculation zone first forms is $Re \approx 5.75$, which is consistent with the low-dimensional Galerkin analysis of Noack & Eckelmann [22]. As Re increases, the wake remains steady and symmetric about its centerline, but eventually transitions – via a supercritical Hopf bifurcation [23] – to an unsteady laminar self-excited state of periodic vortex shedding above a critical value of Re. Williamson [24] determined that critical value to be $Re = 49$, but Dušek *et al.* [25] arrived at a slightly lower value of $Re = 47.1$ via numerical simulations and a truncated Landau model. It is worth noting that the symmetry of the cylinder wake prior to its Hopf bifurcation to an unsteady limit cycle is in stark contrast to the asymmetry observed in the subcritical flow around a sphere [8].

Like that of a sphere, the drag coefficient of a circular cylinder undergoes marked changes at low Reynolds numbers ($0 < Re < 350$) [26, 27]. In the steady regime ($Re \lesssim 47$), the drag coefficient decreases with increasing Re because both the viscous and pressure components of the drag decrease [28]. In the unsteady regime ($Re \gtrsim 47$), however, the pressure component increases with Re, counteracting the decrease in the viscous component to produce an overall increase in the total drag coefficient for $Re \gtrsim 150$ [29].

1.3. Flow around a non-inclined torus ($\theta = 0°$)

Several previous studies have investigated the flow around a torus, but mostly at an inclination angle of zero ($\theta = 0°$) where the torus' axis of rotational symmetry is parallel to the free-stream velocity, as illustrated in Fig. 1(c). Wind-tunnel experiments by Roshko [30] and Monson [31] showed that as the aspect ratio of a non-inclined torus increases, the wake transitions from that of a sphere ($\mathcal{AR} = 0$) to that of a circular cylinder ($\mathcal{AR} = \infty$). The critical value of $\mathcal{AR}$ at which that transition occurs is $\mathcal{AR}_{crit} \approx 3.9$, which was determined by Sheard *et al.* [8, 32] through numerical simulations and linear Floquet analysis. The transition coincides with a change in the scaling relationship between the Strouhal number and Re, but only when the latter is high enough to cause periodic vortex shedding.

To investigate the effect of Re, Leweke & Provansal [33] have conducted wind-tunnel experiments on several different non-inclined tori ($\theta = 0°$). However, they focused mostly on $\mathcal{AR} > 10$, which is above the critical transition ($\mathcal{AR}_{crit} \approx 3.9$ [8, 32]) between sphere-like wakes and cylinder-like wakes. Therefore, they observed behavior fairly similar to that of a cylinder wake. At $Re < 350$, they found three distinct flow regimes: (i) a steady wake at

$Re < 50$, (ii) vortex shedding at $50 < Re < 200$, and (iii) flow transition at $180 < Re < 350$. During vortex shedding, six periodic modes were identified, including parallel and oblique modes. These spatiotemporal dynamics were then successfully modelled with a low-order coupled-oscillator system based on the Ginzburg–Landau equation [33].

At $Re \sim 1$, the Stokes drag on a non-inclined torus can be calculated from the exact solutions of Majumdar & O'Neill [34] and Goren & O'Neill [35] or from the singularity solution of Johnson & Wu [36]. Free-fall experiments [37, 31] and numerical simulations [19] have shown that, as Re increases from 1 to 50, the aspect ratio corresponding to minimum drag decreases from $Æ = 5$ (cylinder-like) to $Æ = 1$ (sphere-like). Sheard *et al.* [19] have proposed an empirical formula for the drag coefficient of a non-inclined torus, which appears as a power-law fit that is valid for $Re < 100$. However, no previous studies have quantified the drag coefficient of an inclined torus, which is the subject of the present study.

1.4. Flow around an inclined torus ($\theta \neq 0°$)

To our knowledge, there has only been one previous study performed on the flow around an inclined torus. Inoue *et al.* [38] experimentally investigated the spatiotemporal dynamics of an inclined torus wake ($Æ = 3$ and 5) at two Reynolds numbers above the onset of vortex shedding: $Re = 600$ and 1500. Using flow visualization and ultrasonic anemometry, they found that the wake dynamics change elaborately as θ changes. At zero inclination ($\theta = 0°$), two different modes of vortex shedding were observed: (i) a disk mode at $Æ = 3$ characterized by an oblique vortex loop and a cylindrical shear layer and (ii) a ring mode at $Æ = 5$ characterized by the formation of counter-rotating vortex rings. However, no difference in the shedding frequency was observed between the two modes. At moderate inclination ($\theta = 45°$), the vortex shedding loses its periodicity owing to nonlinear interactions between vortices shed from the inner and outer surfaces of the torus. At strong inclination ($\theta = 80°$), the interactions between those shed vortices strengthen, leading to lock-in via synchronization [39], a typical feature of self-excited hydrodynamic oscillators [40, 41, 42]. Although this study by Inoue *et al.* [38] has contributed significantly to our understanding of the unsteady behavior of inclined torus wakes, it was performed at Reynolds numbers above the onset of vortex shedding, leaving many open questions about the steady behavior of such wakes, particularly in relation to their recirculation zones and the lift and drag coefficients.

1.5. Contributions of the present study

In this numerical study, we examine the flow around an inclined torus at Reynolds numbers below the onset of vortex shedding: $10 \leqslant Re \leqslant 50$. Our aim is to explore the effect of θ on the steady wake behavior, particularly the size and location of the recirculation zones and the lift and drag coefficients. In Secs. 2 and 3, we present the flow configuration and the numerical framework used in our simulations. In Sec. 4, we validate that numerical framework with two case studies performed on two classical wake flows: the flow around a sphere ($Æ = 0$) and the flow around a non-inclined torus ($Æ = 2$ and 3). In Sec. 5, we present and discuss our findings by examining the wake structure, recirculation zones, and lift and drag coefficients, within a parameter space defined by $Æ$, Re and θ. In Sec. 6, we conclude with the key results and possible directions for future work.

2. Flow configuration

Direct numerical simulations are performed on a steady uniform free-stream of velocity U flowing around a torus inclined at an angle of θ, which is defined as the angle between the free-stream velocity and the torus' axis of rotational symmetry (see Fig. 1d). Several inclination angles ($0° \leqslant \theta \leqslant 90°$) and four aspect ratios ($AR \equiv D/d = 2, 2.3, 2.5, 3$) of the torus are considered. These particular values of AR are chosen because they are in the transitional range between sphere-like behavior and cylinder-like behavior [8, 32].

Three-dimensional viscous incompressible flow is considered, as governed by the Navier–Stokes equations:

$$\partial_t \boldsymbol{u} + \boldsymbol{u} \cdot \nabla \boldsymbol{u} = -\nabla p + \frac{1}{Re} \nabla^2 \boldsymbol{u} \tag{1}$$

$$\nabla \cdot \boldsymbol{u} = 0 \tag{2}$$

where $\boldsymbol{u}$ and p denote the velocity vector and pressure scalar fields, respectively. The Reynolds number is defined as $Re \equiv Ud/\nu$, where U is the free-stream velocity, d is the cross-sectional diameter of the torus (see Fig. 1c), and ν is the kinematic viscosity. The static pressure p is non-dimensionalized by the free-stream dynamic pressure ρU^2, where ρ is the fluid density.

As mentioned in Sec. 1, the focus of our study is on the wake characteristics of an inclined torus at Reynolds numbers low enough for steady flow. The stability analysis of Sheard *et al.* [8, 32] showed that, within the range of aspect ratios considered here ($2 \leqslant AR \leqslant 3$), the bifurcation from steady flow to unsteady flow occurs at $Re \approx 90$. Therefore, we keep $Re \leqslant 50$ to conservatively maintain steady flow, which will be validated in Secs. 3 and 4.

3. Numerical framework

Figure 2 shows the computational domain, whose boundaries are defined by the Cartesian limits of $(\pm L, \pm W, \pm H) = (\pm 30d, \pm 17d, \pm 17d)$. These boundaries are sufficiently far away from the torus to keep the flow uniform in the far field. The torus is positioned at $(x, y, z) = (-L/2, 0, 0)$ with a no-slip condition imposed on its surface. A free-stream condition is imposed on the inlet velocity at the upstream boundary ($x = -L$), a Neumann stress-free condition is imposed on the outlet velocity at the downstream boundary ($x = L$), and a slip condition is imposed on the four lateral boundaries running parallel to the free-stream.

Direct numerical simulations are performed on a 3D hybrid grid. Cartesian background nodes are used for the computational domain, and mesh-free nodes are used for the immersed rigid torus and its immediate surroundings. Spatial discretization is achieved by the combination of (i) a singular value decomposition (SVD) based generalized finite difference (GFD) scheme, which is applied to the mesh-free nodes, and (ii) a conventional finite difference scheme, which is applied to the Cartesian nodes. The SVD–GFD scheme is also applied to a small number of Cartesian nodes having mesh-free nodes in their neighborhood of $[-\Delta x, \Delta x] \times [-\Delta y, \Delta y] \times [-\Delta z, \Delta z]$. The full details of this SVD–GFD scheme have been discussed by Wang *et al.* [43] and Ang *et al.* [44], so only a brief description is given below.

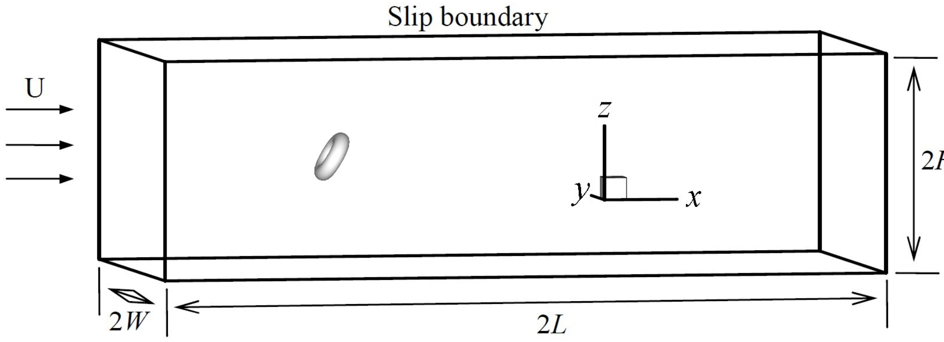

Fig. 2: Computational domain for steady uniform flow at velocity U around a torus inclined at an angle of θ. The size of the computational domain is $(\pm L, \pm W, \pm H) = (\pm 30d, \pm 17d, \pm 17d)$.

The GFD scheme is based on a Taylor series expansion in which the derivative components $\partial f_{19\times 1} = (\partial_x, \partial_y, \partial_z, \partial_x^2, \partial_y^2, ..., \partial_y^3, \partial_z^3)^T f|_{x_0}$ of the function $f(\boldsymbol{x})$ at a reference node $\boldsymbol{x}_0 = (x_0, y_0, z_0)$ are related to its functional values $f_i = f(\boldsymbol{x}_i)$ at n support nodes $\boldsymbol{x}_i = \boldsymbol{x}_i + \Delta\boldsymbol{x}_i (i = 1, ..., n)$ by:

$$\Delta f_{n\times 1} = [S]_{n\times 19}\, \partial f_{19\times 1} \tag{3}$$

where

$$\Delta f_{n\times 1} = (f_1 - f_0, f_2 - f_0, ..., f_n - f_0)^T, \tag{4}$$

$$[S]_{n\times 19} = \begin{bmatrix} \Delta x_1 & \Delta y_1 & \Delta z_1 & 0.5\Delta {x_1}^2 & 0.5\Delta {y_1}^2 & 0.5\Delta {z_1}^2 & ... \\ \Delta x_2 & \Delta y_2 & \Delta z_2 & 0.5\Delta {x_2}^2 & 0.5\Delta {y_2}^2 & 0.5\Delta {z_2}^2 & \\ \Delta x_3 & \Delta y_3 & \Delta z_3 & 0.5\Delta {x_3}^2 & 0.5\Delta {y_3}^2 & 0.5\Delta {z_3}^2 & \\ ... & & & & & & \\ \Delta x_n & \Delta y_n & \Delta z_n & 0.5\Delta {x_n}^2 & 0.5\Delta {y_n}^2 & 0.5\Delta {z_n}^2 & \end{bmatrix}. \tag{5}$$

In general, $n > 19$ support nodes are needed to approximate the second-order derivatives of $\partial f_{19\times 1} = (\partial_x, \partial_y, \partial_z, \partial_x^2, \partial_y^2, ..., \partial_y^3, \partial_z^3)^T f|_{\boldsymbol{x_0}}$ to an accuracy of $\mathcal{O}(|\Delta\boldsymbol{x}|^2)$. The derivatives are calculated by solving the over-determined linear system of Eq. (3) through the use of SVD, which minimizes the L_2-norm (least squares) of the residual error vector. The error components are weighted to give greater importance to nodes closer to the reference node $\boldsymbol{x}_0$. The least-squares solution to Eq. (3) is given by:

$$\partial f_{n\times 1} = [S^W]^+ [W] \Delta f_{n\times 1} \tag{6}$$

where $[S^W]^+$ denotes the pseudo-inverse of the weighted S-matrix $[S^W] = [W][S]_{n\times 9}$ and

$[W]$ is the n weighting (diagonal) matrix, as given by:

$$W = \begin{cases} 2/3 - 4\bar{r}_i^2 + 4\bar{r}_i^3 & \text{for} \quad \bar{r}_i \leqslant 1/2 \\ 4/3 - 4\bar{r}_i + 4\bar{r}_i^2 - 4\bar{r}_i^3/3 & \text{for} \quad 1/2 < \bar{r}_i \leqslant 1 \\ 0 & \text{for} \quad \bar{r}_i > 1 \end{cases} \tag{7}$$

where $\bar{r}_i = |\Delta \boldsymbol{x}_i|/[\max_{j=1,\dots,n} |\Delta \boldsymbol{x}_j|](i = 1, ..., n)$ is the normalized nodal distance.

The governing equations are solved in the time domain using the semi-implicit second-order Crank-Nicolson fractional-step method of Chew *et al.* [45] with modifications made to the boundary conditions [44]. The simulations are performed from $t = 0$ with $\Delta t = 0.025$ until a steady state is reached. A parallel computing technique based on shared memory multi-processors (OpenMP) [46] is used to accelerate the simulations.

After the velocity and pressure fields are computed, the total force vector acting on the torus is found by integrating the local pressure acting over its surface. The total force vector is then projected in the $+x$ and $-z$ directions to get the drag force (F_D) and the lift force (F_L), respectively. The lift force is defined to be positive in the downwards ($-z$) direction because, in this study, inclining the torus by a positive value of θ results in downwards lift (see Fig. 2). From F_D and F_L, the drag and lift coefficients are calculated as:

$$C_D = \frac{F_D}{0.5\rho A_\theta U^2} \tag{8}$$

$$C_L = \frac{F_L}{0.5\rho A_\theta U^2} \tag{9}$$

where A_θ is the projected frontal area of the torus. Both the drag and lift forces are made up of the sum of a pressure component and a viscous component: $F_D = F_{Dp} + F_{Dv}$ and $F_L = F_{Lp} + F_{Lv}$. In Sec. 5, these will be examined together with C_D and C_L.

4. Validation of the numerical framework

The numerical framework presented in Sec. 3 is validated through two case studies performed on two classical wake flows: (i) the flow around a sphere and (ii) the flow around a non-inclined torus.

4.1. Validation case study (i): Flow around a sphere

In the first case study, the flow around a sphere is examined in the steady flow regime at $10 \leqslant Re \leqslant 200$ [10, 11, 18]. The Reynolds number is defined here as $Re \equiv UD_s/\nu$, where D_s is the diameter of the sphere, U is the free-stream velocity, and ν is the kinematic viscosity. The computational domain is a 3D rectangular box with dimensions of $30D_s \times 15D_s \times 15D_s$, which is discretized into $221 \times 131 \times 131$ Cartesian nodes. The Cartesian grid is uniform in all three spatial directions within a $4D_s \times 2D_s \times 2D_s$ box containing the sphere, with a grid spacing of $\Delta x = \Delta y = \Delta z = 0.04D_s$. The surface of the sphere is discretized into 2966 mesh-free nodes. Four more layers of mesh-free nodes are placed radially away from the surface, with a smaller radial spacing used for nodes closer to the surface. The distance between the surface and the first layer of nodes is $0.017D_s$. Preliminary numerical testing has confirmed that this mesh is fine enough to produce grid-independent results.

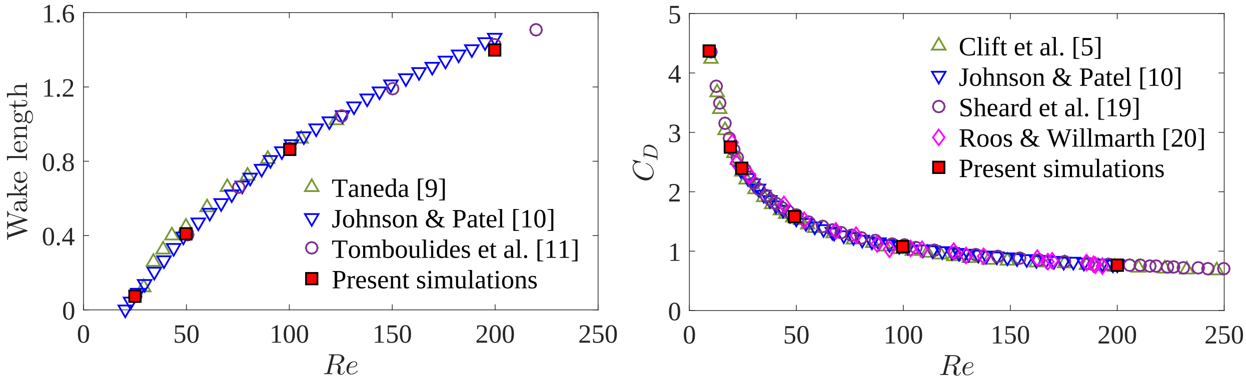

(a) Length of the recirculating wake

(b) Drag coefficient

Fig. 3: Numerical validation on the steady flow around a sphere at $10 \leqslant Re \leqslant 250$.

Figure 3 compares our simulations with numerical and experimental data from the literature. It can be seen that for $10 \leqslant Re \leqslant 250$ (a) a steady recirculating wake forms behind the sphere at $Re \approx 20$ and elongates with increasing Re, and (b) the drag coefficient first decreases sharply and then more gradually as Re increases. These findings are in excellent quantitative agreement with reference data from the literature [5, 9, 10, 11, 19, 20], validating our numerical framework.

4.2. Validation case study (ii): Flow around a non-inclined torus

In the second case study, the flow around a non-inclined torus ($Æ = 2$ and 3) is examined in the steady flow regime at $10 \leqslant Re \leqslant 50$ [8, 32, 33]. The computational domain is a 3D rectangular box with dimensions of $60d \times 34d \times 34d$, which is discretized into $231 \times 181 \times 181$ Cartesian nodes. The Cartesian grid is uniform in all three spatial directions within a $6d \times 6d \times 6d$ box containing the torus, with a grid spacing of $\Delta x = \Delta y = \Delta z = 0.06d$. The surface of the torus is discretized into 5420 mesh-free nodes for $Æ = 2$ and into 8068 mesh-free nodes for $Æ = 3$. Four more layers of mesh-free nodes are placed radially away from the surface, with a smaller radial spacing used for nodes closer to the surface. The distance between the surface and the first layer of nodes is $0.026d$. Preliminary numerical testing has confirmed that this mesh is fine enough to produce grid-independent results.

Figures 4 and 5 show the streamlines of the flow in the x–y plane at $Æ = 2$ and 3, respectively. In both figures, our 3D SVD–GFD simulations are compared against simulations performed in axisymmetric coordinates using an alternative numerical scheme based on the finite volume method (FVM) of Yu *et al.* [47, 48]. For the present values of Re and $Æ$, the comparison shows excellent agreement. Furthermore, the streamlines are consistent with those reported by Sheard *et al.* [8], whose stability analysis predicts that the flow is steady and axisymmetric for the present values of Re and $A\!\!\!R$. The wake structure can be seen to change markedly as Re increases. Behind the $A\!\!\!R = 2$ torus, a detached recirculation zone develops near the flow centerline at $Re = 10$ (Fig. 4a,b), but it grows and moves downstream when Re increases to 50 (Fig. 4c,d), leaving behind a second smaller recirculation zone attached to the back of the torus. Behind the $A\!\!\!R = 3$ torus, there is no recirculation zone at $Re = 10$ (Fig. 5a,b), but a small attached one forms at $Re = 20$ (Fig. 5c,d). At $Re = 50$ (Fig. 5e,f), a second recirculation zone appears behind the outer edge of the first, which becomes elongated in the streamwise direction. Unlike the first recirculation zone, however, this second one is detached from the torus. The broad agreement in streamline patterns between our 3D SVD–GFD method, our axisymmetric FVM method, and the results of Sheard *et al.* [8] is further validation of our numerical framework.

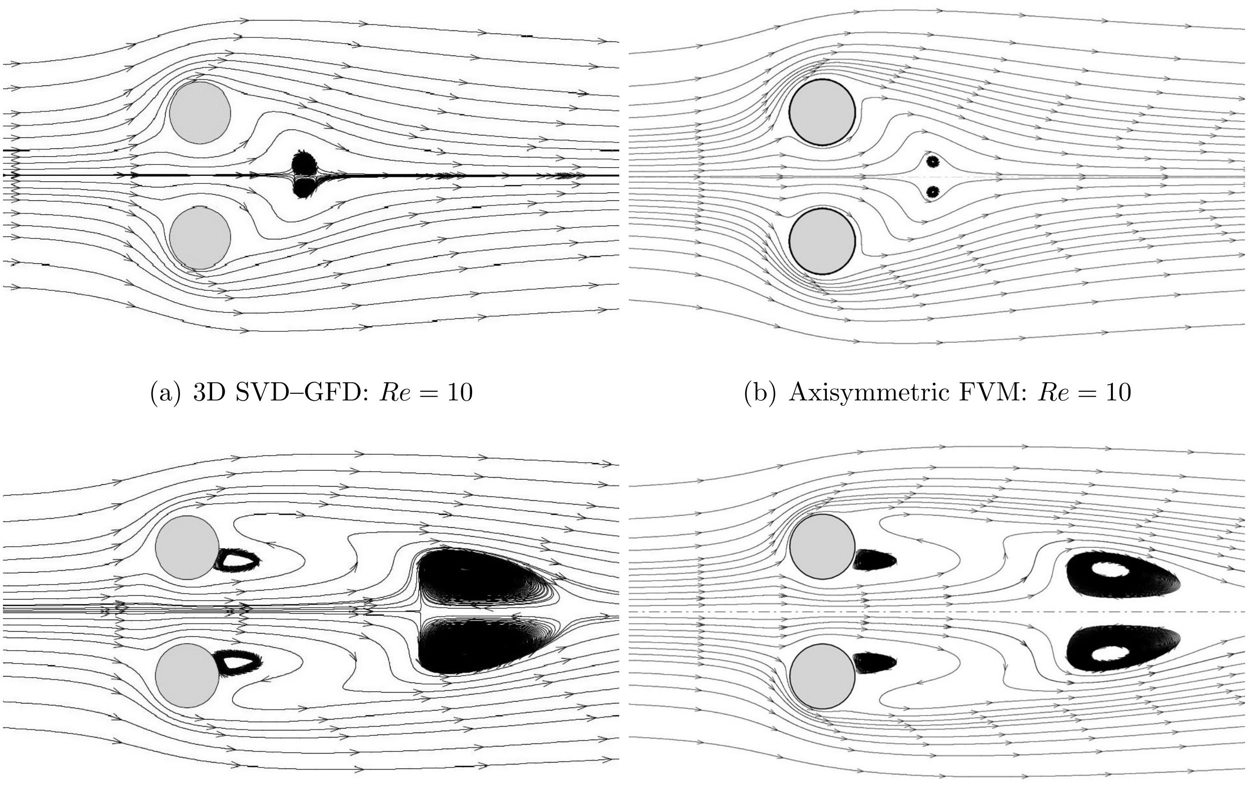

(a) 3D SVD–GFD: $Re = 10$

(b) Axisymmetric FVM: $Re = 10$

(c) 3D SVD–GFD: $Re = 50$

(d) Axisymmetric FVM: $Re = 50$

Fig. 4: Numerical validation on the steady flow around a non-inclined torus at $A\!\!\!R = 2$: (a,c) 3D SVD–GFD simulations and (b,d) axisymmetric FVM simulations. Shown are streamlines in the x–y plane at two Reynolds numbers: (a,b) $Re = 10$ and (c,d) $Re = 50$.

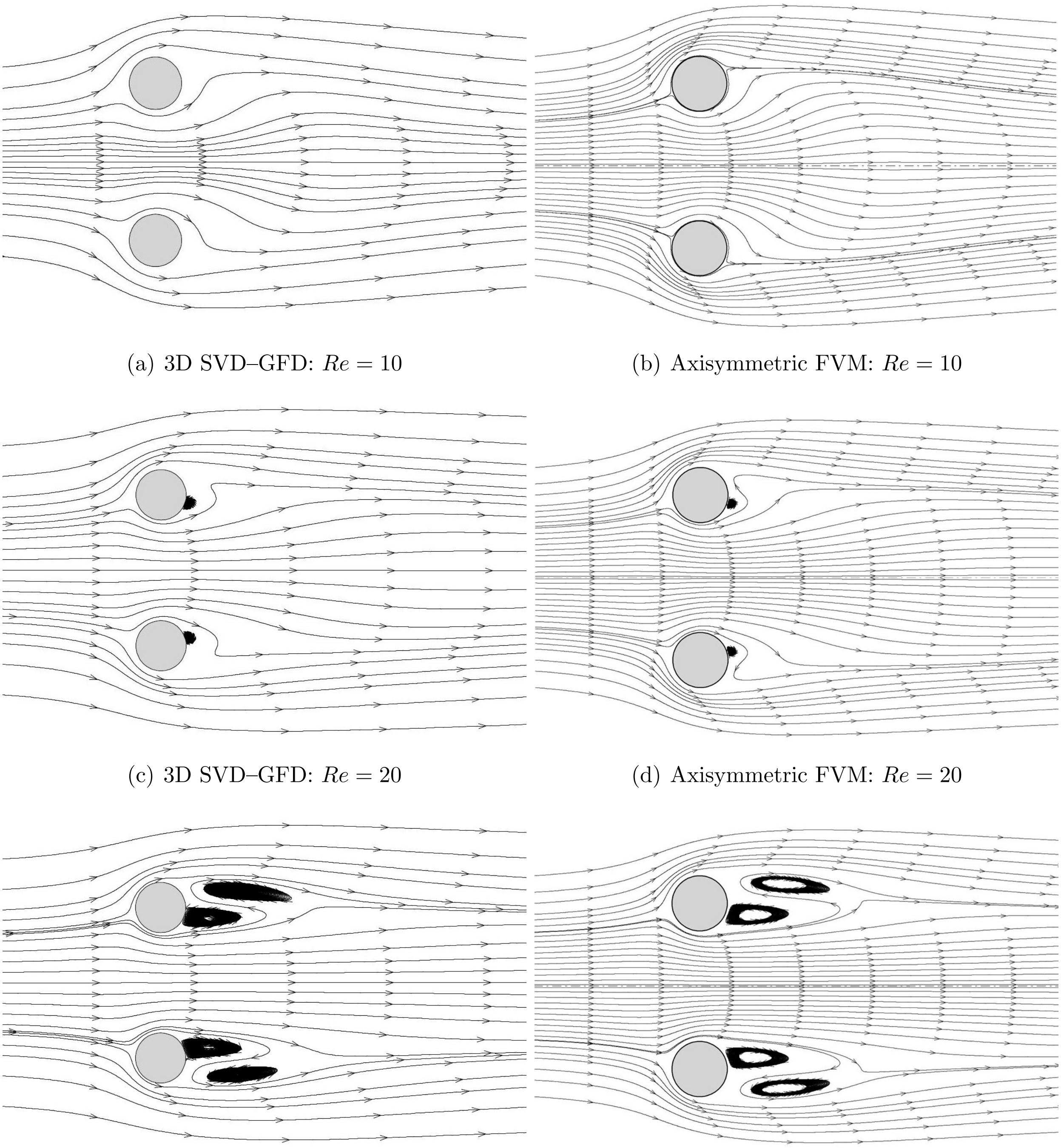

(a) 3D SVD–GFD: $Re = 10$

(b) Axisymmetric FVM: $Re = 10$

(c) 3D SVD–GFD: $Re = 20$

(d) Axisymmetric FVM: $Re = 20$

(e) 3D SVD–GFD: $Re = 50$

(f) Axisymmetric FVM: $Re = 50$

Fig. 5: Numerical validation on the steady flow around a non-inclined torus at $\AE = 3$: (a,c,e) 3D SVD–GFD simulations and (b,d,f) axisymmetric FVM simulations. Shown are streamlines in the x–y plane at three Reynolds numbers: (a,b) $Re = 10$, (c,d) $Re = 20$ and (e,f) $Re = 50$.

For a more quantitative comparison, Table 1 lists the non-dimensional distances between the central plane of a non-inclined $\text{Æ} = 2$ torus and the front and rear stagnation points of its rearmost recirculation zone at two Reynolds numbers: $Re = 25$ and 50. For both values of Re, the agreement between our 3D SVD–GFD simulations and our axisymmetric FVM simulations is within 0.55%, further validating our numerical framework.

Table 1: Numerical validation on the steady flow around a non-inclined torus at $\text{Æ} = 2$: non-dimensional distance from the central plane of the torus to the front and rear stagnation points of its rearmost recirculation zone at two Reynolds numbers.

	$Re = 25$		$Re = 50$	
	Front	Rear	Front	Rear
3D SVD–GFD simulations	1.762	4.116	3.688	6.004
Axisymmetric FVM simulations	1.762	4.112	3.707	6.010

As a final validation step, Fig. 6 shows the drag coefficient (C_D) of a non-inclined torus at $Re \leqslant 160$ for $\text{Æ} = 2$ and 3. For both values of Æ, as Re increases from around 10, C_D first decreases sharply but then levels off as the flow transitions from being viscous-dominated to being pressure-dominated. This is the same trend observed in the C_D of a sphere ($\text{Æ} = 0$) [5, 10, 11]. As before, there is excellent quantitative agreement between the three independent numerical schemes: our 3D SVD–GFD simulations, our axisymmetric FVM simulations, and the axisymmetric simulations of Sheard *et al.* [19]. This agreement shows that our numerical framework is capable of accurately simulating the steady flow around a bluff body at low Re. In the next section, we will use this numerical framework to investigate the steady flow around an inclined torus at similarly low Re.

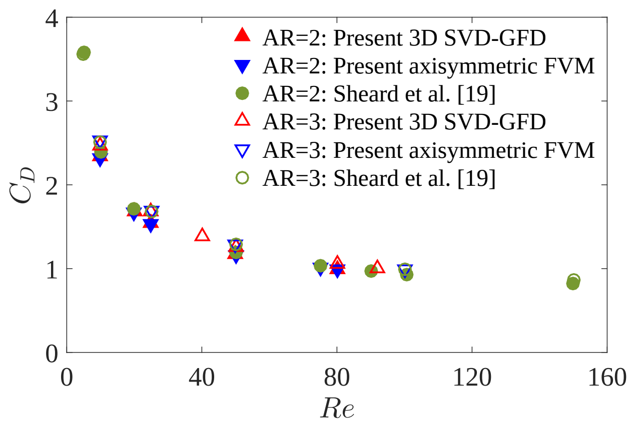

Fig. 6: Comparison of the drag coefficient of a non-inclined torus ($\text{Æ} = 2$ and 3) at $Re \leqslant 160$ across three independent numerical schemes.

5. Results and discussion

5.1. *Effect of the inclination angle*

First we examine the effect of θ on the steady wake behavior, focusing on the drag and lift coefficients and on how they are influenced by the structure of the recirculation zone.

5.1.1. *Drag and lift coefficients*

Figure 7 shows the drag and lift coefficients of an inclined $AR = 2$ torus as a function of θ at four Reynolds numbers: $Re = 10$, 20, 25 and 50. As the torus inclines (i.e. as θ increases), C_D decreases monotonically from a maximum at $\theta = 0°$ to a minimum at $\theta = 90°$ (full inclination). Meanwhile, C_L starts from zero at $\theta = 0°$ because of top-down symmetry about the y-axis, reaches a maximum at $40° \leqslant \theta \leqslant 50°$, and then returns to zero at $\theta = 90°$ because of a return to top-down symmetry. As Re increases, both C_D and C_L decrease; similar decreases have been observed in the flow around a circular cylinder [26, 28]. The decrease in C_D is uniform across all values of θ, but the decrease in C_L is concentrated at intermediate values of θ, where the torus has the least top-down symmetry about the y-axis.

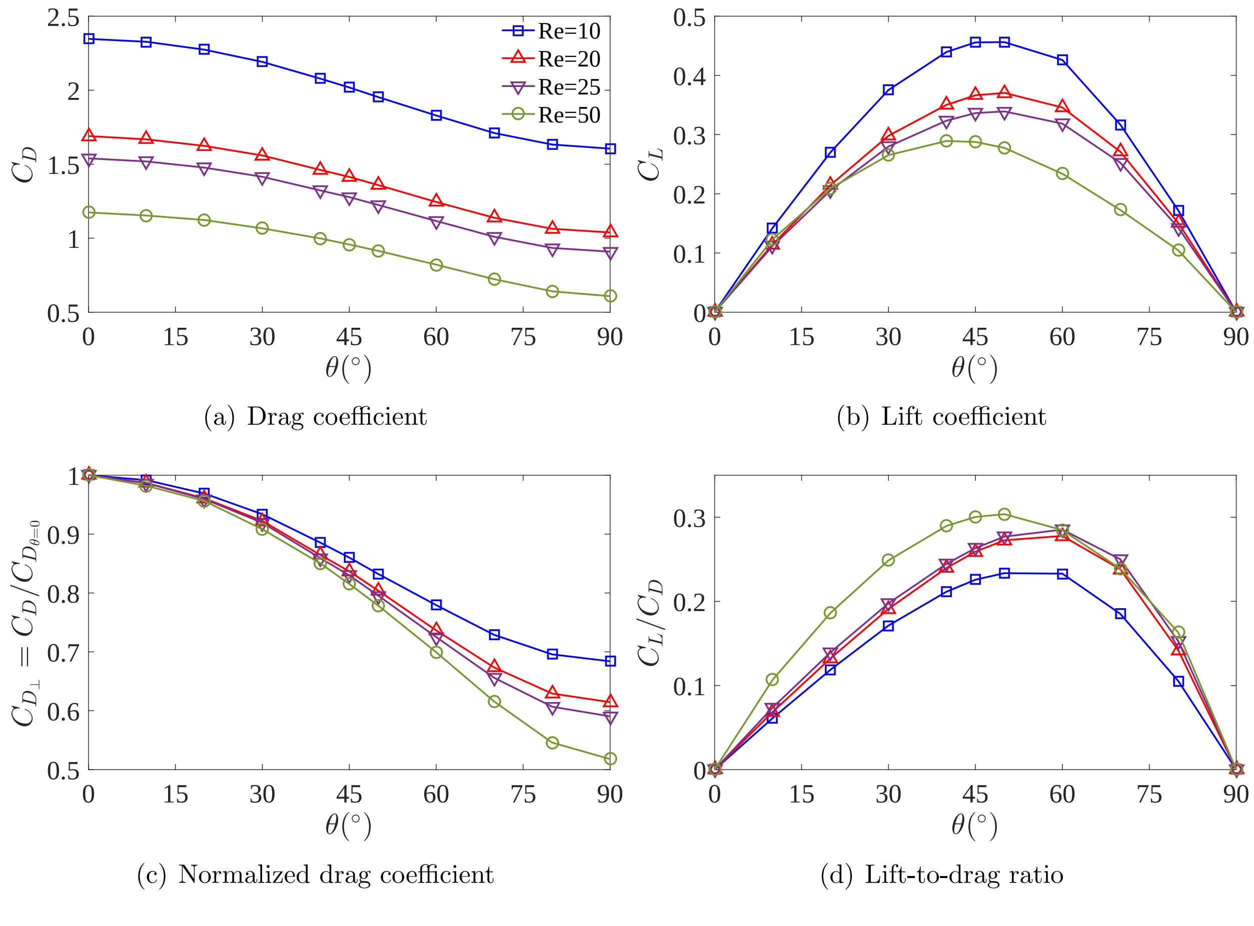

(a) Drag coefficient

(b) Lift coefficient

(c) Normalized drag coefficient

(d) Lift-to-drag ratio

Fig. 7: (a) Drag coefficient, (b) lift coefficient, (c) normalized drag coefficient, and (d) lift-to-drag ratio as a function of θ for steady flow around an inclined $AR = 2$ torus at four Reynolds numbers.

The decrease in C_D with θ is compared across different values of Re by normalizing C_D by its maximum value, which occurs at $\theta = 0°$: $C_{D_\perp} = C_D/C_{D_{\theta=0}}$. As can be seen from Fig. 7(c), the decrease in the normalized $C_{D_\perp}$ with θ becomes more pronounced as Re increases. By fitting quartic polynomials to the $C_{D_\perp} - \theta$ curves, we find that the location of the inflection point shifts to higher θ as Re increases: from $\theta = 51.8°$ at $Re = 10$ to $\theta = 59.1°$ at $Re = 50$. This contrasts with the behavior seen in inclined circular cylinders, where the inflection point always occurs at an inclination angle of approximately 45° [28].

Figure 7(d) shows C_L/C_D as a function of θ. The overall trends are similar to those of C_L versus θ: as θ increases for a fixed Re, C_L/C_D starts from zero at zero inclination ($\theta = 0°$), increases to a maximum at moderate inclination, and then returns to zero at full inclination ($\theta = 90°$). There are, however, two notable differences: (i) because C_D decreases with increasing θ, the critical value of θ at which C_L/C_D peaks is generally larger than that at which C_L peaks, and (ii) because C_D decreases more rapidly than C_L does with increasing Re, C_L/C_D ends up increasing with Re, despite C_L itself decreasing with increasing Re.

Figure 8(a) shows the pressure (C_{Dp}) and viscous (C_{Dv}) components of the total drag coefficient at the flow conditions of Fig. 7. At small θ, the pressure drag exceeds the viscous drag for all values of Re. However, as θ increases, the pressure drag decreases monotonically, falling below the viscous drag, which remains relatively constant with θ. The critical value of θ at which the pressure drag balances the viscous drag increases with Re because the latter decreases slightly more than the former does as Re increases. These findings show that the decrease in the total drag (C_D) with θ seen in Fig. 7 is due primarily to a decrease in the pressure drag (C_{Dp}) with almost no change in the viscous drag (C_{Dv}).

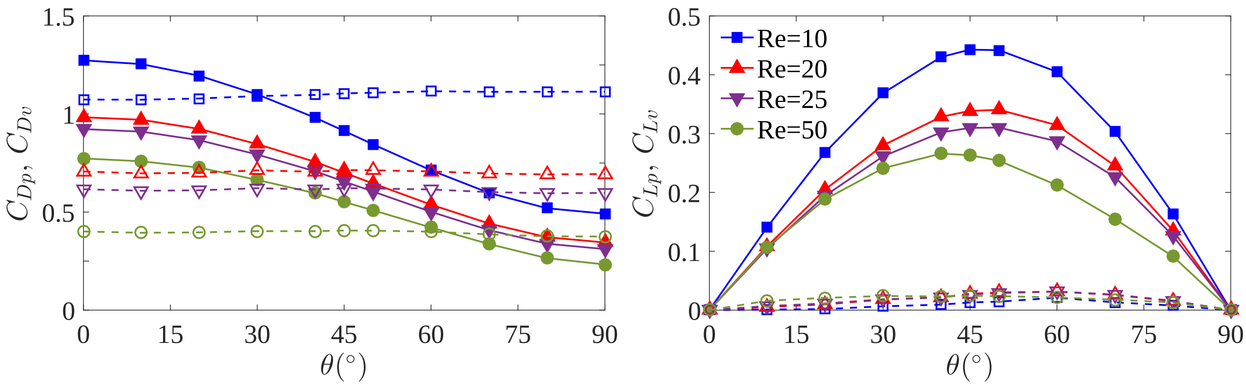

(a) Drag coefficient

(b) Lift coefficient

Fig. 8: The pressure and viscous components of (a) the drag coefficient and (b) the lift coefficient as a function of θ for steady flow around an inclined $Æ = 2$ torus at four Reynolds numbers. The solid lines/filled markers denote the pressure components, and the dashed lines/hollow markers denote the viscous components.

Figure 8(b) shows the pressure (C_{Lp}) and viscous (C_{Lv}) components of the total lift coefficient. Across all values of θ, the pressure lift dominates the viscous lift, making up over 85% of the total lift regardless of Re. The viscous lift makes up the remainder of the total lift and is invariably small because the shear stresses acting on the torus surface are aligned predominately with the free-stream, perpendicular to the lift direction.

5.1.2. Wake structure

To explore the physical cause of the decrease in C_D with θ, we show in Fig. 9 streamlines from the x–y and x–z planes for steady flow around an $Æ = 2$ torus at $Re = 50$ and four inclination angles: (a) $\theta = 10°$, (b) $\theta = 30°$, (c) $\theta = 45°$, and (d) $\theta = 60°$.

At $\theta = 10°$ (Fig. 9a), the outer streamlines diverge, wrap around the torus, and then converge downstream. In the x–y plane, there are two distinct recirculation zones on either side of the flow centerline: a large detached zone and a small attached zone. These are similar to those observed behind a non-inclined torus at $1 \leqslant Æ \leqslant 2$ [8] (see also Fig. 4c,d). In the x–z plane, there are two recirculation zones in total, both of which are located behind the upper (leeward trailing) section of the inclined torus.

As θ increases (Fig. 9b–d), the small attached recirculation zone in the x–y plane disappears, and the initially large detached recirculation zone behind it shrinks and moves upstream, becoming attached to the torus when $\theta = 60°$. In the x–z plane, the two distinct recirculation zones merge and move behind the hole of the torus. In general, recirculation zones are regions of low pressure. When they disappear, shrink or move away from the surface of a bluff body, the static pressure behind that body tends to increase, reducing the pressure imbalance between the front stagnation point and the rear wake. This reconfiguration of the recirculation zones could explain why the pressure drag and C_D decrease with increasing θ, as seen in Sec. 5.1.1. Another contributing factor could be the sheltering effect that the lower (windward leading) section of the torus has on the upper (leeward trailing) section [49]. This effect is analogous to that which occurs in the flow around two circular cylinders arranged in a tandem configuration, for which the drag coefficient is known to decrease as the two cylinders approach each other [50]. One may imagine the flow around an inclined torus as being similar to that around two short cylinders arranged in an offset-tandem configuration. Numerical simulations by Lee *et al.* [51] have shown that the two cylinders need not be in perfect tandem (i.e. θ need not be perfectly 90°) for there to be a drag reduction. For a cylinder-to-cylinder spacing equivalent to that of an $Æ = 2$ torus, Lee *et al.* [51] found that C_D starts to decrease at $\theta \approx 30°$ and continues to decrease all the way to $\theta = 90°$ [51], which is consistent with the C_D trends observed in Fig. 7.

To further explore the changes occurring in the wake structure, we turn to 3D streamlines of the flow at $\theta = 45°$, as shown in Fig. 10. At $Re = 10$ (Fig. 10a), there is no evidence of a recirculation zone. The flow passing through the hole of the torus emerges from the back without recirculating and then moves downstream. At $Re = 25$ (Fig. 10b), a small recirculation zone develops immediately downstream of the torus. At $Re = 50$ (Fig. 10c), the recirculation zone grows in the streamwise direction. This can be seen in the streamline pattern as well as in the change in sign (from positive to negative) of the local pressure coefficient (C_p) on the inner-upstream surface of the torus as Re increases from 25 to 50 (Fig. 10b–c). Previous research by Yu *et al.* [52] focusing on the velocity profile of the flow around a non-inclined torus ($\theta = 0°$) has shown that when Re increases from 1 to 70, the maximum velocity increases and its location shifts closer to the torus. This could explain why C_p on the inner wall is negative, and why the location and growth of the recirculation zone change with increasing Re. Farther downstream, the recirculating fluid is faster on the upper side of the torus than it is on the lower side, as evidenced by the diverging streamlines.

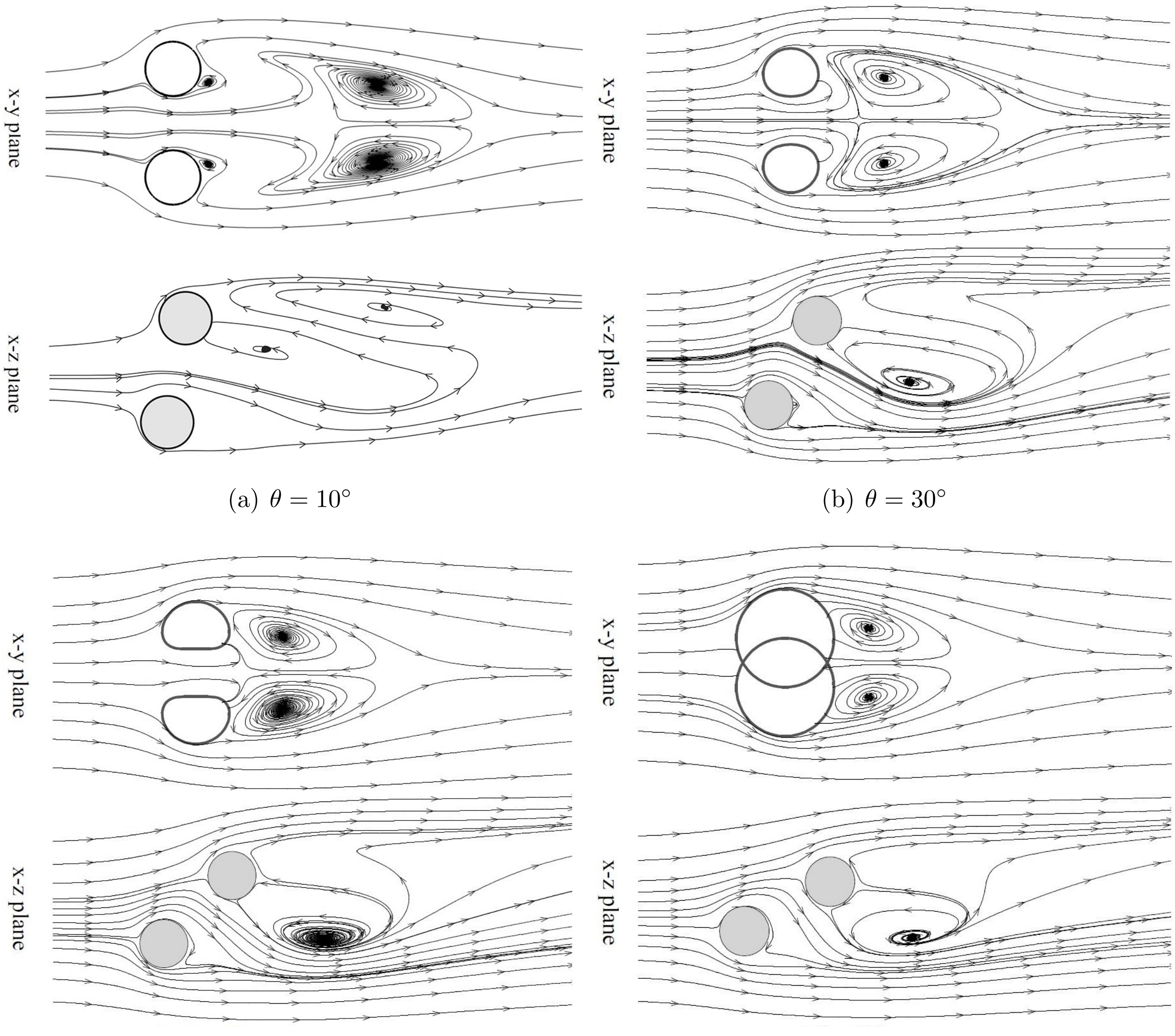

(a) $\theta = 10°$ (b) $\theta = 30°$

(c) $\theta = 45°$ (d) $\theta = 60°$

Fig. 9: Streamlines of the steady flow around an $Æ = 2$ torus at $Re = 50$ for four inclination angles: (a) $\theta = 10°$, (b) $\theta = 30°$, (c) $\theta = 45°$, and (d) $\theta = 60°$.

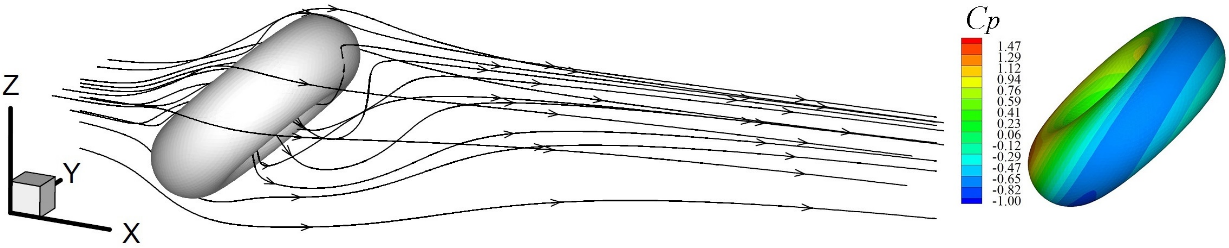

(a) $Re = 10$

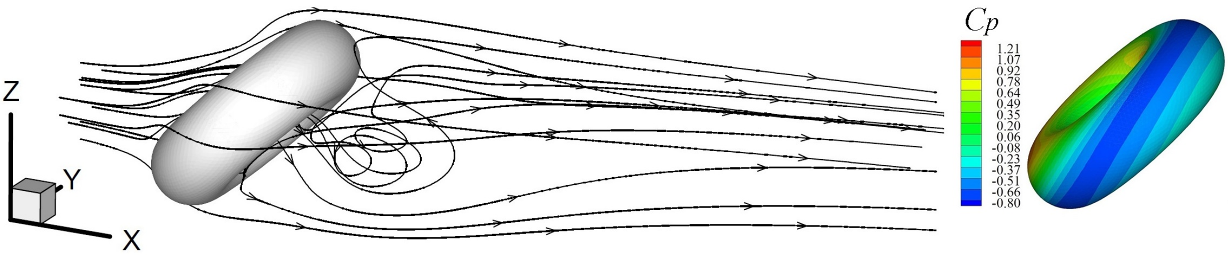

(b) $Re = 25$

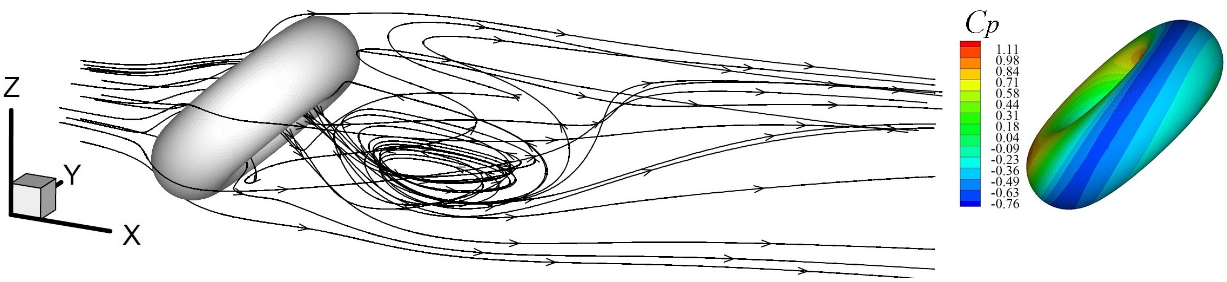

(c) $Re = 50$

Fig. 10: (left) 3D streamlines and (right) local pressure coefficient of the steady flow around an $\mathcal{R} = 2$ torus at $\theta = 45°$ for three Reynolds numbers: (a) $Re = 10$, (b) $Re = 25$, and (c) $Re = 50$.

5.2. Effect of the aspect ratio

Next we examine the effect of $\mathcal{R}$ on the drag and lift coefficients.

5.2.1. Drag and lift coefficients

Figure 11(a–b) shows the drag and lift coefficients at three aspect ratios ($\mathcal{R} = 2$, 2.5, 3) and three Reynolds numbers ($Re = 10$, 25, 50). For most flow conditions, C_D and C_L are only weakly sensitive to $\mathcal{R}$. At zero inclination ($\theta = 0°$), C_D for $\mathcal{R} = 3$ is around 5% ($Re = 10$) to 8% ($Re = 50$) higher than that for $\mathcal{R} = 2$. At full inclination ($\theta = 90°$), C_D for $\mathcal{R} = 3$ is around 8% ($Re = 50$) to 10% ($Re = 10$) lower than that for $\mathcal{R} = 2$. Thus, there is a critical value of θ above which C_D for $\mathcal{R} = 2$ overtakes that for $\mathcal{R} = 3$. This critical angle is around 50° when $Re = 10$ but is over 70° when $Re = 50$. Interestingly, C_L is much less sensitive to $\mathcal{R}$ when $Re = 10$ or 50 than when $Re = 25$, where C_L for $\mathcal{R} = 2$ consistently exceeds that for $\mathcal{R} = 3$ over an intermediate range of inclination angles, $45° \leqslant \theta \leqslant 80°$.

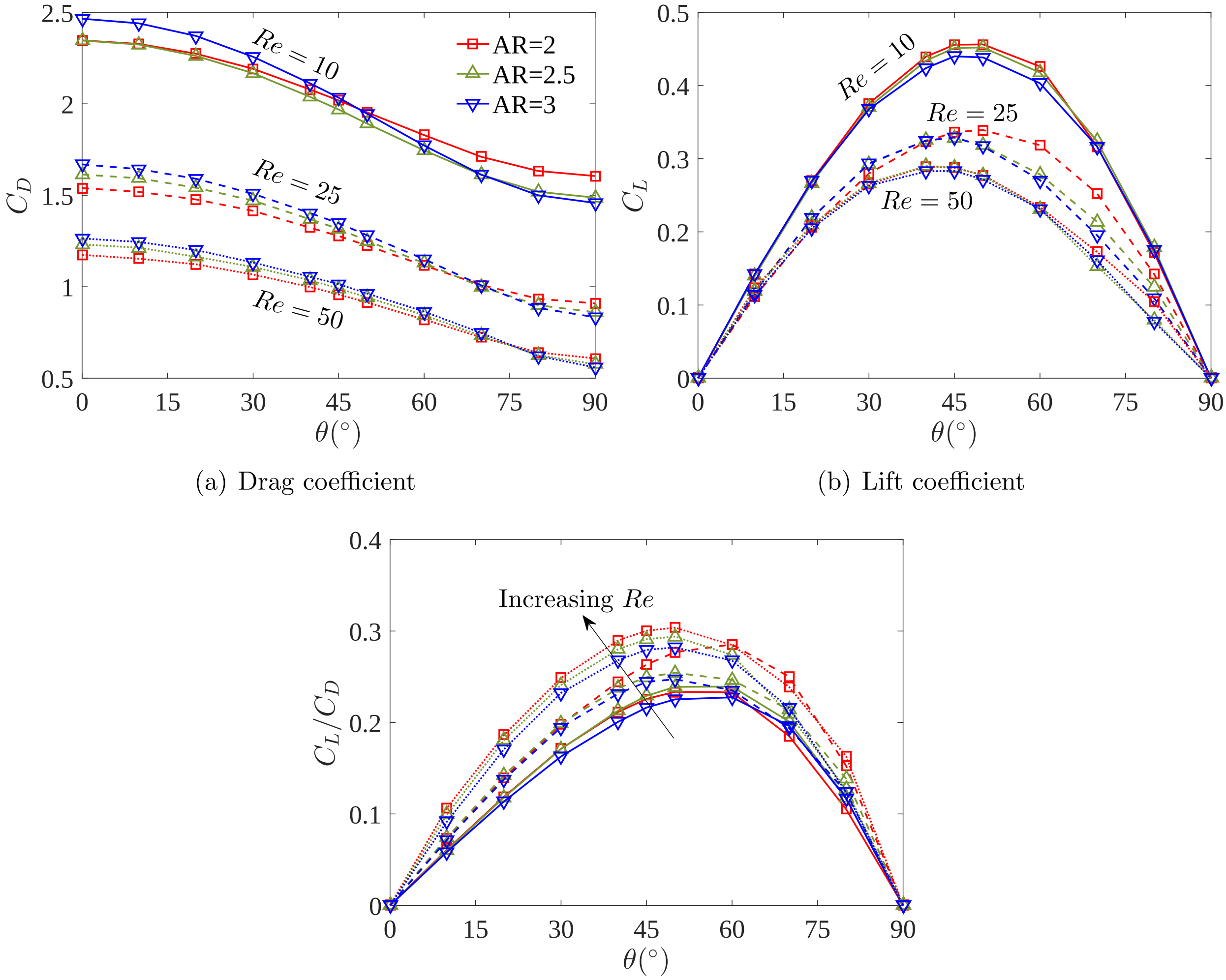

(a) Drag coefficient

(b) Lift coefficient

(c) Lift-to-drag ratio

Fig. 11: (a) Drag coefficient, (b) lift coefficient and (c) lift-to-drag ratio as a function of θ for steady flow around an inclined torus at three aspect ratios and three Reynolds numbers: (solid lines) $Re = 10$, (dashed lines) $Re = 25$, and (dotted lines) $Re = 50$.

Figure 11(c) shows the lift-to-drag ratio, which combines the overall trends of C_D and C_L. The maximum difference in C_L/C_D caused by variations in Æ increases and shifts to higher θ as Re increases, starting from less than 4% for $Re = 10$ ($\theta = 40°$), increasing to 29% for $Re = 25$ ($\theta = 70°$), and then saturating to around 28% for $Re = 50$ ($\theta = 80°$). As with Fig. 7(d), C_L/C_D increases with Re because C_D decreases more rapidly than C_L does.

Figure 12(a) shows the pressure (C_{Dp}) and viscous (C_{Dv}) components of the total drag coefficient. Only data for $Re = 50$ are shown because it is representative of the other values of Re. The overall trends are similar to those of Fig. 8(a), where C_{Dp} decreases monotonically as θ increases, while C_{Dv} remains relatively constant. This leads to C_{Dp} dominating C_{Dv} at small θ but then being overtaken by C_{Dv} at large θ. In Fig. 12(a), the contribution of

C_{Dp} to C_D for $\mathit{AR} = 3$ is slightly higher than that for $\mathit{AR} = 2$, with the maximum difference being around 2% at zero inclination ($\theta = 0°$). These findings show that, for $2 \leqslant \mathit{AR} \leqslant 3$, the decrease in the total drag (C_D) observed as θ increases can be attributed mainly to a decrease in the pressure drag (C_{Dp}) rather than to changes in the viscous drag (C_{Dv}).

Figure 12(b) shows the pressure (C_{Lp}) and viscous (C_{Lv}) components of the total lift coefficient at $Re = 50$. For $2 \leqslant \mathit{AR} \leqslant 3$, C_{Lp} dominates C_{Lv} at all values of θ because the shear stresses acting on the torus surface are aligned mainly parallel to the free-stream velocity, perpendicular to the lift vector.

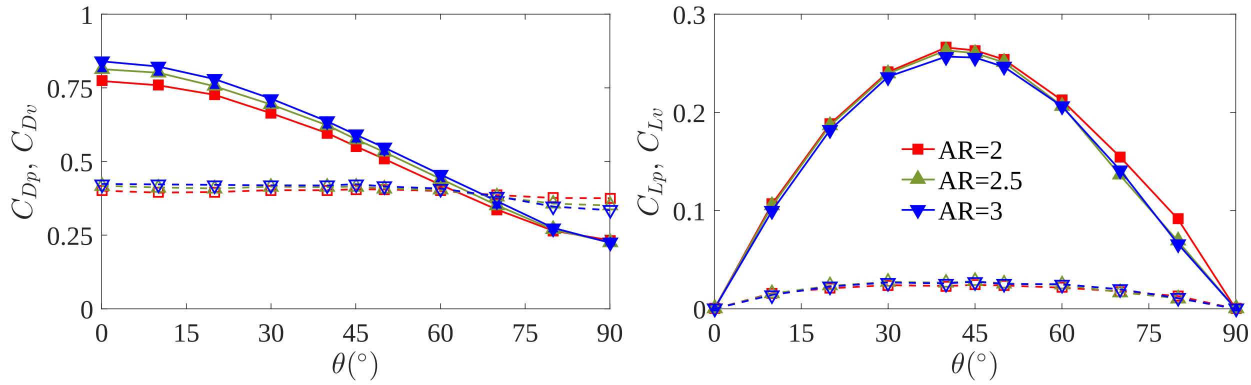

(a) Drag coefficient

(b) Lift coefficient

Fig. 12: The pressure and viscous components of (a) the drag coefficient and (b) the lift coefficient as a function of θ for steady flow around an inclined $\mathit{AR} = 2$ torus at $Re = 50$. The solid lines/filled markers denote the pressure components, and the dashed lines/hollow markers denote the viscous components.

5.3. Nonlinear regression analysis of C_D and C_L

A nonlinear regression analysis is performed to give curve fits for C_D and C_L as a function of three independent variables: (i) the aspect ratio, $2 \leqslant \mathit{AR} \leqslant 3$, (ii) the inclination angle, $0 \leqslant \theta \leqslant 90°$, and (iii) the Reynolds number, $10 \leqslant Re \leqslant 50$. These fits can be used to model the drag and lift forces acting on a torus in reduced-order simulations where the detailed flow around the torus need not be explicitly resolved, reducing the computational costs [53].

Table 2 lists the regression models and their coefficients for the curve fits to C_D and C_L. These fits were generated with MATLAB's `nlinfit` function, which uses an iterative least squares algorithm to calculate the robust weights using the residual from the preceding iteration [54]. The form of the model for C_D was chosen based on the observation that C_D decreases with θ similarly to the cosine function. The independent variable Re is included as an additive term because its effect does not vary significantly with θ or AR and so can be decoupled. The form of the model for C_L was chosen based on the observation that C_L increases and decreases with θ similarly to the sine function. For both models, the coefficient of determination (R^2) is high, with values of $R^2 = 0.988$ for C_D and $R^2 = 0.987$ for C_L.

Also shown in Table 2 is the root mean square (RMS) difference between our numerical simulations and nonlinear regression analysis. Across $2 \leqslant \mathit{AR} \leqslant 3$, the RMS difference is

4.61% for C_D and 8.16% for C_L, both of which compare favorably with previous numerical simulations on the steady flow around an inclined circular cylinder [28]. As AR increases from 2 to 3, the RMS difference in C_D increases monotonically but that in C_L remains relatively constant. To visualize this, we show in Fig. 13 the drag and lift coefficients calculated by our numerical simulations and those approximated by the curve fits. Overall there is good agreement, consistent with the data in Table 2.

Table 2: Nonlinear regression analysis on the steady flow around an inclined torus. Shown are curve fits for the drag coefficient (C_D) and lift coefficient (C_L) as a function of three independent variables: (i) the aspect ratio, $2 \leqslant AR \leqslant 3$, (ii) the inclination angle, $0 \leqslant \theta \leqslant 90^\circ$, and (iii) the Reynolds number, $10 \leqslant Re \leqslant 50$.

	Model	Coefficients	R^2	RMS Difference
Drag	$C_D = \beta_1 AR^{\beta_2} \cos(2\theta) + \beta_3 Re^{\beta_4}$	$\beta_1 = 0.207485$ $\beta_2 = 0.626308$ $\beta_3 = 5.781323$ $\beta_4 = -0.468003$	0.988	4.61% for $AR = 2$–3 3.32% for $AR = 2$ 3.91% for $AR = 2.3$ 4.71% for $AR = 2.5$ 5.63% for $AR = 3$
Lift	$C_L = \gamma_1 AR^{\gamma_2} Re^{\gamma_3} \sin(2\theta)$	$\gamma_1 = -0.987067$ $\gamma_2 = -0.115132$ $\gamma_3 = -0.298905$	0.987	8.16% for $AR = 2$–3 8.62% for $AR = 2$ 8.27% for $AR = 2.3$ 8.51% for $AR = 2.5$ 7.48% for $AR = 3$

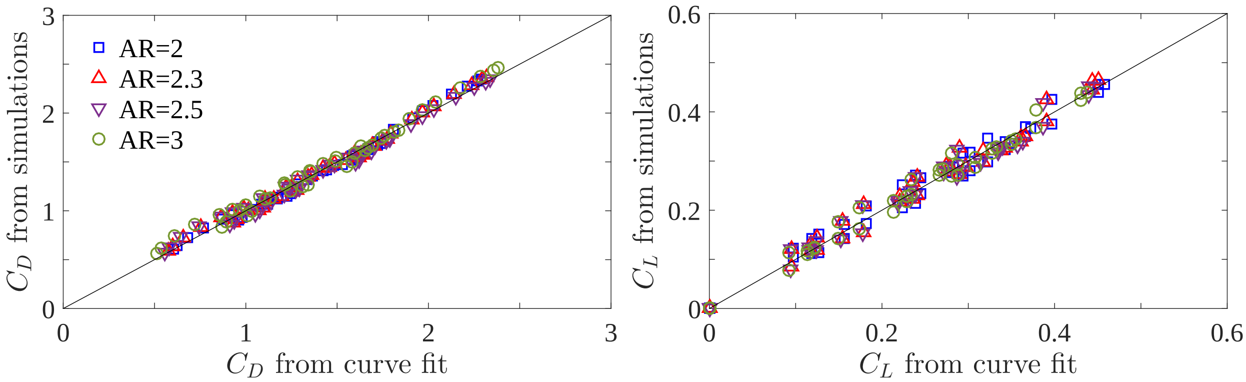

(a) Drag coefficient (b) Lift coefficient

Fig. 13: Comparison of the drag and lift coefficients between our numerical simulations and the nonlinear regression analysis of Table 2.

6. Conclusions

Using a 3D SVD–GFD scheme, we have performed direct numerical simulations of the steady flow around an inclined torus over a range of aspect ratios ($2 \leqslant AR \leqslant 3$), inclination angles ($0 \leqslant \theta \leqslant 90°$) and Reynolds numbers ($10 \leqslant Re \leqslant 50$). We examined the drag (C_D) and lift (C_L) coefficients of the torus and related their trends to the physical structure of the recirculation zones. We then performed a nonlinear regression analysis to generate curve fits for C_D and C_L in terms of Æ, θ and Re. Our focus was on the steady flow regime – at Reynolds numbers below the onset of vortex shedding – because that regime had not been explored before but is relevant to many engineering and biological situations, such as the sedimentation of particles and the motion of natural micro-swimmers such as helical flagella.

For a fixed Re, it was found that as the torus inclines from a flow-normal orientation ($\theta = 0°$) to a flow-parallel orientation ($\theta = 90°$), C_D decreases monotonically, while C_L first increases from zero, reaches a maximum at $40° \leqslant \theta \leqslant 50°$ and then returns to zero owing to top-down symmetry at full inclination. The decrease in C_D with θ was attributed to a decrease in the pressure drag, with almost no change in the viscous drag. The variation in C_L with θ was attributed to the pressure lift dominating the viscous lift, with the latter making up less than 15% of the total lift because the shear stresses acting on the torus surface are aligned mainly with the free-stream, perpendicular to the lift vector. With increasing Re, the overall trends in C_D and C_L remain qualitatively unchanged but their quantitative values decrease – much as they do in the flow around a circular cylinder. Compared with the effects of θ and Re, those of Æ are relatively weak for the particular flow conditions examined in this study. Curve fits to C_D and C_L in terms of Æ, θ and Re were found to be in good agreement with the numerical data, with an RMS difference of less than 9% and $R^2 \geqslant 0.987$. Future work could involve extending the present simulations to higher Reynolds numbers where a series of nonlinear bifurcations to unsteady flow is expected to occur.

Acknowledgements

This work was supported by the Research Grants Council of Hong Kong (Project Nos. 16235716 and 26202815). WH would like to acknowledge the support provided by the China Scholarship Council during his studies in Madrid. PY would like to thank the Special Program for Applied Research on Super Computation of the NSFC–Guangdong Joint Fund (second phase) under Grant No. U1501501.

References

[1] C. Williamson, Vortex dynamics in the cylinder wake, Annual Review of Fluid Mechanics 28 (1) (1996) 477–539.

[2] L. Wang, Z. Guo, J. Mi, Drafting, kissing and tumbling process of two particles with different sizes, Computers & Fluids 96 (2014) 20–34.

[3] Y.-C. Cho, W. Shyy, Adaptive control of low-Reynolds number aerodynamics in uncertain environments: Part 1. Disturbance regimes and flow characteristics, Computers & Fluids 86 (2013) 582–596.

[4] M. Zdravkovich, Flow Around Circular cylinders. A Comprehensive Guide Through Flow Phenomena, Experiments, Applications, Mathematical Models, and Computer Simulations, Vol. 1, Oxford University Press, 1997.

[5] R. Clift, J. Grace, M. Weber, Bubbles, Drops, and Particles, Courier Corporation, 2005.

[6] D. Prabhanjan, G. Raghavan, T. Rennie, Comparison of heat transfer rates between a straight tube heat exchanger and a helically coiled heat exchanger, International Communications in Heat and Mass Transfer 29 (2) (2002) 185–191.

[7] A. F. Tabak, S. Yesilyurt, Computationally-validated surrogate models for optimal geometric design of bio-inspired swimming robots: Helical swimmers, Computers & Fluids 99 (2014) 190–198.
[8] G. Sheard, M. Thompson, K. Hourigan, From spheres to circular cylinders: The stability and flow structures of bluff ring wakes, Journal of Fluid Mechanics 492 (2003) 147–180.
[9] S. Taneda, Experimental investigation of the wake behind a sphere at low Reynolds numbers, Journal of the Physical Society of Japan 11 (10) (1956) 1104–1108.
[10] T. Johnson, V. Patel, Flow past a sphere up to a Reynolds number of 300, Journal of Fluid Mechanics 378 (1999) 19–70.
[11] A. Tomboulides, S. Orszag, Numerical investigation of transitional and weak turbulent flow past a sphere, Journal of Fluid Mechanics 416 (1) (2000) 45–73.
[12] G. G. Stokes, On the effect of the internal friction of fluids on the motion of pendulums, Vol. 9, Pitt Press, 1851, Transactions of the Cambridge Philosophical Society.
[13] H. Lamb, Hydrodynamics, Cambridge University Press, 1932.
[14] C. W. Oseen, Über die stoke'sche formel und über eine verwandte aufgabe in der hydrodynamik, Almqvist & Wiksell, 1911.
[15] G. K. Batchelor, An Introduction to Fluid Dynamics, Cambridge University Press, 2000.
[16] J. Wu, G. Faeth, Sphere wakes in still surroundings at intermediate Reynolds numbers, AIAA journal 31 (8) (1993) 1448–1455.
[17] B. Fornberg, Steady viscous flow past a sphere at high Reynolds numbers, Journal of Fluid Mechanics 190 (1) (1988) 471.
[18] R. Natarajan, A. Acrivos, The instability of the steady flow past spheres and disks, Journal of Fluid Mechanics 254 (1993) 323–344.
[19] G. Sheard, K. Hourigan, M. Thompson, Computations of the drag coefficients for low-Reynolds-number flow past rings, Journal of Fluid Mechanics 526 (2005) 257–275.
[20] F. Roos, W. Willmarth, Some experimental results on sphere and disk drag, AIAA Journal 9 (2) (1971) 285–291.
[21] R. Underwood, Calculation of incompressible flow past a circular cylinder at moderate Reynolds numbers, Journal of Fluid Mechanics 37 (01) (1969) 95–114.
[22] B. Noack, H. Eckelmann, A low-dimensional Galerkin method for the three-dimensional flow around a circular cylinder, Physics of Fluids 6 (1) (1994) 124–143.
[23] M. Provansal, C. Mathis, L. Boyer, Bénard-von kármán instability: Transient and forced regimes, Journal of Fluid Mechanics 182 (1) (1987) 1.
[24] C. Williamson, Defining a universal and continuous Strouhal–Reynolds number relationship for the laminar vortex shedding of a circular cylinder, Physics of Fluids 31 (10) (1988) 2742–2744.
[25] J. Dušek, P. Le Gal, P. Fraunié, A numerical and theoretical study of the first Hopf bifurcation in a cylinder wake, Journal of Fluid Mechanics 264 (1994) 59–80.
[26] R. Henderson, Details of the drag curve near the onset of vortex shedding, Physics of Fluids 7 (9) (1995) 2102–2104.
[27] R. Henderson, Nonlinear dynamics and pattern formation in turbulent wake transition, Journal of Fluid Mechanics 352 (1997) 65–112.
[28] A. Vakil, S. I. Green, Drag and lift coefficients of inclined finite circular cylinders at moderate Reynolds numbers, Computers & Fluids 38 (9) (2009) 1771–1781.
[29] C. Williamson, A. Roshko, Measurements of base pressure in the wake of a cylinder at low Reynolds numbers, Zeitschrift fur Flugwissenschaften und Weltraumforschung 14 (1990) 38–46.
[30] A. Roshko, On the development of turbulent wakes from vortex streets.
[31] D. Monson, The effect of transverse curvature on the drag and vortex shedding of elongated bluff bodies at low Reynolds number, Journal of fluids engineering 105 (3) (1983) 308–318.
[32] G. Sheard, M. Thompson, K. Hourigan, From spheres to circular cylinders: Non-axisymmetric transitions in the flow past rings, Journal of Fluid Mechanics 506 (2004) 45–78.
[33] T. Leweke, M. Provansal, The flow behind rings: Bluff body wakes without end effects, Journal of Fluid Mechanics 288 (1995) 265–310.

[34] S. Majumdar, M. O'Neill, On axisymmetric Stokes flow past a torus, Zeitschrift für angewandte Mathematik und Physik ZAMP 28 (4) (1977) 541–550.
[35] S. Goren, M. O'Neill, Asymmetric creeping motion of an open torus, Journal of Fluid Mechanics 101 (01) (1980) 97–110.
[36] R. Johnson, T. Wu, Hydromechanics of low-Reynolds-number flow: Motion of a slender torus, Journal of Fluid Mechanics 95 (02) (1979) 263–277.
[37] A. Amarakoon, R. Hussey, B. Good, E. Grimsal, Drag measurements for axisymmetric motion of a torus at low Reynolds number, Physics of Fluids 25 (9) (1982) 1495–1501.
[38] Y. Inoue, S. Yamashita, M. Kumada, An experimental study on a wake of a torus using UVP monitor, Experiments in Fluids.
[39] A. Pikovsky, M. Rosenblum, J. Kurths, Synchronization: A universal concept in nonlinear sciences, Vol. 12, Cambridge university press, 2003.
[40] L. Li, M. Juniper, Lock-in and quasiperiodicity in hydrodynamically self-excited flames: Experiments and modelling, P. Combust. Inst. 34 (1) (2013) 947–954.
[41] L. Li, M. Juniper, Lock-in and quasiperiodicity in a forced hydrodynamically self-excited jet, J. Fluid Mech. 726 (2013) 624–655.
[42] L. Li, M. Juniper, Phase trapping and slipping in a forced hydrodynamically self-excited jet, J. Fluid Mech. 735 (R5) (2013) 1–11.
[43] X. Wang, K. Yeo, C. Chew, B. Khoo, A SVD-GFD scheme for computing 3D incompressible viscous fluid flows, Computers & Fluids 37 (6) (2008) 733–746.
[44] S. Ang, K. Yeo, C. Chew, C. Shu, A singular-value decomposition (SVD)-based generalized finite difference (GFD) method for close-interaction moving boundary flow problems, International Journal for Numerical Methods in Engineering 76 (12) (2008) 1892–1929.
[45] C. Chew, K. Yeo, C. Shu, A generalized finite-difference (GFD) ALE scheme for incompressible flows around moving solid bodies on hybrid meshfree–Cartesian grids, Journal of Computational Physics 218 (2) (2006) 510–548.
[46] R. Chandra, Parallel programming in OpenMP, Morgan Kaufmann, 2001.
[47] P. Yu, T. Lee, Y. Zeng, H. Low, A numerical method for flows in porous and homogenous fluid domains coupled at the interface by stress jump, International Journal for Numerical Methods in Fluids 53 (11) (2007) 1755–1775.
[48] P. Yu, T. Lee, Y. Zeng, S. Meguid, H. Low, A numerical technique for laminar swirling flow at the interface between porous and homogenous fluid domains, International Journal for Numerical Methods in Fluids 60 (3) (2009) 337–353.
[49] K. Lee, K.-S. Yang, Flow patterns past two circular cylinders in proximity, Computers & Fluids 38 (4) (2009) 778–788.
[50] B. Sharman, F.-S. Lien, L. Davidson, C. Norberg, Numerical predictions of low Reynolds number flows over two tandem circular cylinders, International Journal for Numerical Methods in Fluids 47 (5) (2005) 423–447.
[51] K. Lee, K.-S. Yang, D.-H. Yoon, Flow-induced forces on two circular cylinders in proximity, Computers & Fluids 38 (1) (2009) 111–120.
[52] P. Yu, Steady flow past a torus with aspect ratio less than 5, Journal of Fluids and Structures 48 (2014) 393–406.
[53] A. H. Nayfeh, F. Owis, M. R. Hajj, A model for the coupled lift and drag on a circular cylinder, ASME Paper No. DETC2003/VIB-48455.
[54] P. W. Holland, R. E. Welsch, Robust regression using iteratively reweighted least-squares, Communications in Statistics-theory and Methods 6 (9) (1977) 813–827.